








Cite this: *J. Mater. Chem. C*, 2022, 10, 5934

## Engineering mesophase stability and structure *via* incorporation of cyclic terminal groups†

Richard J. Mandle, \*<sup>ab</sup> Laurence C. Abbott, <sup>a</sup> Luma Fritsch, <sup>ac</sup> Rachel R. Parker, <sup>a</sup> Sam Hart,<sup>a</sup> Adrian C. Whitwood, <sup>a</sup> Stephen J. Cowling, <sup>a</sup> John N. Moore <sup>a</sup> and John W. Goodby<sup>a</sup>

We report on the characterisation of a number of liquid-crystalline materials featuring cyclic terminal groups, which lead to significant enhancements in the temperature range of the mesomorphic state. Materials with only short terminal chains are able to support lamellar mesophase formation by appending a large terminal cyclic unit at the end of a short spacer composed of methylene units. X-ray scattering experiments reveal that the layer spacings of the lamellar smectic phase are significantly larger when a cyclic end-group is present than for equivalent linear unsubstituted materials, but there is no effect on orientational order. Fully atomistic molecular dynamics simulations faithfully reproduce experimental layer spacings and orientational order parameters, and indicate that the cyclic terminal units spontaneously segregate into diffuse sub-layers and thus cause the increased layer spacing. This shape segregation predicted by molecular dynamics simulations is observed in the crystalline solid state by X-ray diffraction.

Received 13th December 2021,  
Accepted 16th February 2022

DOI: 10.1039/d1tc05954h

rsc.li/materials-c

## Introduction

Liquid crystals for display applications typically comprise a rigid ‘core’ unit flanked with a terminal chain and a polar terminal group. The need to engineer the properties of nematic liquid-crystals has led to an understanding of how changes to molecular structure impact the bulk properties of these materials. Positioning a bulky group at the end of the terminal chain can lead to reductions in melting points with only minimal change in the clearing point,<sup>1–7</sup> electron-withdrawing end groups (–Cl, –Br, –ArF<sub>n</sub>) can suppress the SmA mesophase of cyanobiphenyl derived LCs<sup>8</sup> although in phenylpyrimidine-derived materials these halogen terminated end groups can actually stabilise the SmA state.<sup>9</sup> Apolar or weakly polar bulky terminal groups (–C(CH<sub>3</sub>)<sub>3</sub> etc.) suppress the nematic phase and lead to smectogenic materials, albeit with reductions in the clearing point relative to the parent material.<sup>4,5</sup> The smectic layer spacing of materials incorporating apolar bulky terminal groups is inversely dependent on temperature.<sup>5</sup>

Some archaea incorporate cyclic units in their lipids<sup>10</sup> which confers, *inter alia*, the ability to withstand greater extremes of temperature than eukaryotes<sup>11</sup> by either raising the temperature at which the liquid crystalline lipid-bilayers undergo isotropisation,<sup>12,13</sup> or lowering the temperature at which they undergo crystallisation.<sup>14,15</sup> Inspired by this, we considered that incorporating cyclic units into the terminal regions of liquid crystalline materials could perhaps offer a similar thermal advantage. Cyclic end groups have previously been studied in the context of the tilted smectic C phase for use in display devices,<sup>16,17</sup> but not for nematic or SmA type materials (Fig. 1) which is the focus of this present article. Furthermore, in prior examples<sup>16,17</sup> the bulky cyclic group is attached to the terminal chain *via* polar groups (esters, ethers), and thus it is difficult to determine to what extent steric and electronic effects are responsible for the resulting behaviour.

Using the 4-cyanobiphenyl mesogenic core unit, in this work we have studied different combinations of ring size, alkyl chain length and linking-unit and their impact on the mesomorphic behaviour of the resulting materials. In our materials the cyclic unit is installed at the terminus of the chain, which is in contrast to archaeal lipids which typically have the cyclic units within the chains. In all cases the cyclic group was directly attached to the alkyl chain and can be described as non-polar; we can therefore attribute any changes in behaviour solely to steric factors. Some cyclic terminal groups were found to give significant enhancements to the transition temperatures relative to the linear unsubstituted parent compounds, to induce

<sup>a</sup> Department of Chemistry, University of York, York, YO10 5DD, UK.  
E-mail: r.mandle@leeds.ac.uk

<sup>b</sup> School of Physics and Astronomy, University of Leeds, Leeds, LS2 9JT, UK

<sup>c</sup> Instituto de Química, Universidade Federal do Rio Grande do Sul, Porto Alegre, RS, Brazil

† Electronic supplementary information (ESI) available. CCDC 2128187–2128191. For ESI and crystallographic data in CIF or other electronic format see DOI: 10.1039/d1tc05954h





**Fig. 1** Cartoon depictions of the sub types of the smectic A phase: monolayer ( $SmA_1$ ), interdigitated ( $SmA_d$ ) and bilayer ( $SmA_2$ ). The molecules are indicated as cylinders with an aspect ratio of 10, the molecular length ( $L$ ) and layer spacing ( $d$ ) are indicated. The layers are shown as transparent planes, however in reality they are diffuse and disordered rather than being well defined.

smectic phases for relatively short terminal chain lengths, as well as leading to anomalously large smectic layer spacings and strong odd-even effects.

## Experimental

Compound **1** was prepared *via* the Furukawa modification of the Simmons–Smith cyclopropanation<sup>18</sup> of 4-(pent-4-enyloxy)-4'-cyanobiphenyl. Compound **2** was obtained *via* the metallophotoredox C–C coupling<sup>19</sup> of 4-(3-bromopropoxy)-4'-cyanobiphenyl with cyclobutanecarboxylic acid. Compounds **3–5** were prepared *via* Mitsunobu etherification<sup>20</sup> of 4-hydroxy-4'-cyanobiphenyl with an appropriate cycloalkyl-terminated alcohol; 3-cyclopentylpropan-1-ol and 3-cyclohexylpropan-1-ol were sourced commercially and used to synthesise **3** and **4**, respectively. For **5**, alkyl–alkyl cross coupling<sup>21</sup> of the redox active *N*-hydroxyphthalimide ester of cycloheptanoic acid with (3-ethoxy-3-oxopropyl)zinc bromide, followed by reduction with LAH, to afford 3-cycloheptylpropan-1-ol. The structures of compounds **1–5** were confirmed by single crystal X-ray diffraction and are shown in Scheme 1 as thermal ellipsoid models (50% probability). Single crystal X-ray diffraction data were collected at 110 K on an Oxford Diffraction SuperNova diffractometer with Cu-K $\alpha$  radiation ( $\lambda = 1.54184 \text{ \AA}$ ) using an EOS CCD camera; further information is given in the ESI<sup>†</sup> to this article.

Compounds **6–10** (Scheme 2) were prepared *via* Mitsunobu etherification of 4-hydroxy-4'-cyanobiphenyl with an appropriate cyclohexyl-terminated alcohol; these were sourced commercially with the exceptions of cyclohexylpentan-1-ol (prepared according to ref. 22) and 6-cyclohexylhexan-1-ol (prepared according to ref. 23). Compound **11** (Scheme 2) was prepared *via* esterification of commercially available 5-cyclohexylpentanoic

acid with 4-hydroxy-4'-cyanobiphenyl using EDC/DMAP. Full synthetic details for all transformations are given in the ESI<sup>†</sup>.

Transition temperatures were determined by polarised optical microscopy (POM, photomicrographs in ESI<sup>†</sup>) and differential scanning calorimetry (DSC) with additional small angle X-ray scattering (SAXS) studies on selected compounds. Numerical integration of X-ray scattering data was performed in Matlab. Electronic structure calculations were performed in Gaussian G09 rev E01,<sup>24</sup> individual conformers were aligned using the VMD software package<sup>25</sup> and rendered using Qutemol.<sup>26</sup> Details of the molecular dynamics (MD) simulation methods are given in the ESI<sup>†</sup>.

## Results

The transition temperatures and associated enthalpies of transition of **1–5**, in which the spacer is held at three methylene units while the size of the terminal ring is varied, are presented along with the analogous linear material (5OCB) in Table 1.

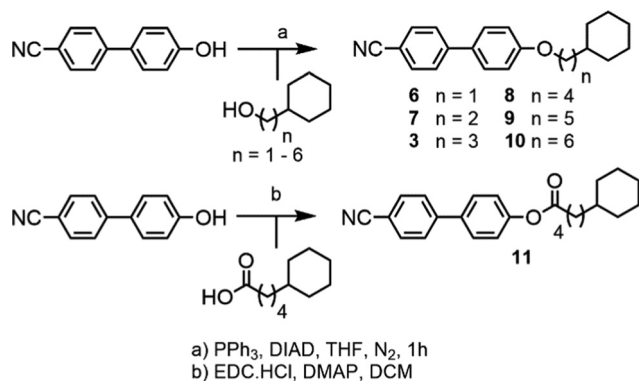
Whereas compounds **1** and **2** exhibit reductions in clearing points relative to 5OCB we observe that materials with larger cyclic end groups (**3–5**) exhibit clearing points notably higher than those of 5OCB. To a first approximation, the clearing points correlate with the ring strain of the cyclic end-group; cyclopropane has the lowest clearing point and highest ring strain, whereas cyclohexane has the highest clearing point and lowest ring strain. However, as we will show, conformational and size-exclusion effects are the underlying cause of this enhancement, rather than ring strain. This enhancement in clearing point is accompanied by an increase in melting point – compounds **1–5** exhibit higher melting points than the linear parent (5OCB). All five novel materials exhibit nematic phases; however it is surprising to observe a smectic A phase in **5** given the short terminal chain employed. The end-to-end length of all-*trans* **5** is only slightly larger than 5OCB (18.8 Å *versus* 17.0 Å, both at the B3LYP/6-31G(d,p) level of DFT). The layer spacing of the  $SmA$  phase of **5** was measured to be 31.0 Å and temperature independent when studied by SAXS. The  $d/l$  ratio (layer spacing over all-*trans* molecular length) is therefore 1.65 for **5**, this being significantly larger than would be expected for a material with a linear alkoxy chain; for example 8OCB (4-octyloxy-4'-cyanobiphenyl) has a  $d/l$  ratio of 1.43.<sup>27</sup> The  $SmA$  phase of **5** is therefore interdigitated and thus of the subtype ' $SmA_d$ ', This interdigitation is common for cyanobiphenyls and results from having molecules form dynamic antiparallel associated pairs through dipole–dipole interactions.<sup>28</sup>

The constituent molecules of the antiparallel cyanobiphenyl pairs rotate about their long axis in the  $SmA$  phase – both independently and cooperatively<sup>29</sup> – meaning that the time averaged shape of the individual molecules is rod like. To estimate the gross shape of **4** and **5** we obtained optimized geometries at the B3LYP/6-31G(d) level of DFT for both materials before optimizing the geometries of conformers that arise from ring flips or twist-boat states. Geometries not within 20 kJ mol<sup>-1</sup> of the global minima were discarded, and those





Scheme 1



Scheme 2

**Table 1** The transition temperatures ( $T$ , °C) and associated enthalpies ( $\Delta H$ ,  $\text{kJ mol}^{-1}$ ) of compounds **1–5**, as determined by DSC at a heat/cool rate of  $10\text{ °C min}^{-1}$ : Values of 5OCB are given for comparison, and were determined by the same method using the same instrument

		MP	SmA <sub>d</sub> -N	N-Iso
5OCB	$T$	48.4	—	68.4
( $n = 0$ )	$\Delta H$	23.7	—	0.4
<b>1</b>	$T$	82.2	—	47.6
( $n = 1$ )	$\Delta H$	26.3	—	0.2
<b>2</b>	$T$	76.4	—	61.5
( $n = 2$ )	$\Delta H$	23.9	—	0.3
<b>3</b>	$T$	89.8	—	74.7
( $n = 3$ )	$\Delta H$	27.1	—	0.5
<b>4</b>	$T$	94.8	—	84.0
( $n = 4$ )	$\Delta H$	28.9	—	0.6
<b>5</b>	$T$	85.0	64.9	73.7
( $n = 5$ )	$\Delta H$	21.1	0.1	0.4

within this limit were overlaid (Fig. 2a for **4** and Fig. 2b for **5**). This gives a more realistic picture of the likely gross shape of the terminal group than afforded by a single conformer, and the volume occupied by the terminal group is larger than that of the biphenyl core unit; hence, the molecules are more conical than rod like (Fig. 2b). The layer spacing of **5** is significantly larger than materials with linear terminal chains; we propose that the steric bulk of the cyclic group suppresses the interpenetration of the terminal alkyl chains into adjacent layers and leads to the enhanced layer spacing (Fig. 2c, d). The observed increases in transition temperatures in compounds **1–5** can be considered as resulting from the better filling of free volume by materials with bulky end groups than linear chains due to the conical, rather than rod-like, shape.<sup>30,31</sup> Indeed, in the crystalline state (Fig. 2e) the bulky cyclic groups of **5** are

clearly segregated from the 4-cyanobiphenyl regions, giving alternating planes of aromatic and alicyclic regions. The XRD crystal structure of compounds **1**, **2** and **4** exhibit similar segregation into cycloalkyl rich planes and biphenyl rich planes (Fig. S8, S9, S11 in ESI†). This segregation is also present for **3**, albeit less pronounced than for compounds **2**, **4** and **5** (Fig. S10 in ESI†).

We next studied the effect of the length of the methylene spacer between the cyanobiphenyl 'core' and the cyclic end-group upon the liquid crystalline properties (Table 2). We



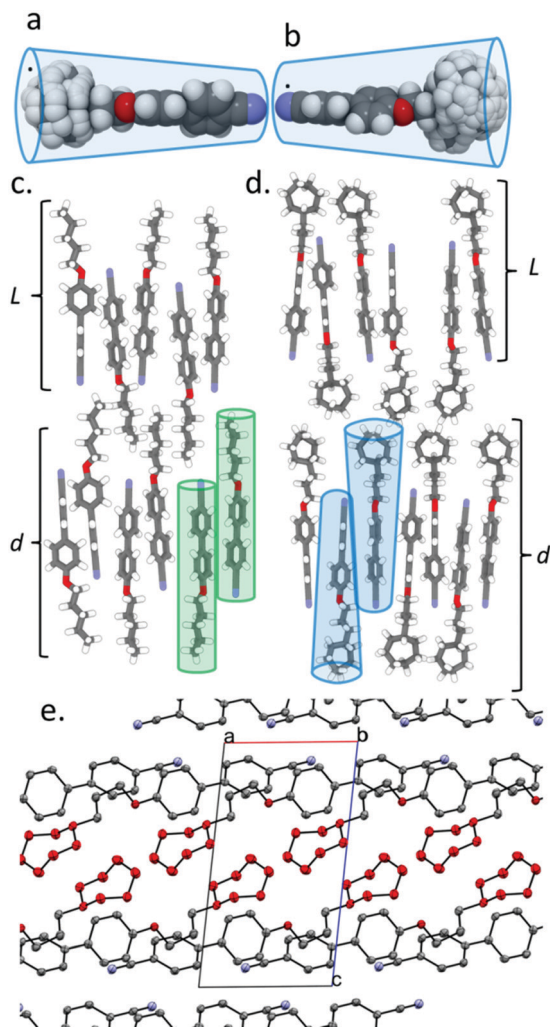


Fig. 2 Overlaid geometries (DFT; B3LYP/6-31G(d)) of conformers within 20 kJ mol<sup>-1</sup> of the global minimum energy geometry for (a) compound **4** and (b) compound **5** obtained by allowing ring flips and twist-boat forms but keeping the methylene chain and biphenyl rigid. Depiction of the SmA<sub>d</sub> phase exhibited by (c) a linear alkoxybiphenyl, (d) a cyanobiphenyl with a terminal group (compound **5**). Rod-like (c) and conical (d) molecular shapes are indicated. (e) Packing in the solid state of **5** as determined by single crystal XRD; a, b and c refer to the axes of the unit cell (*P*1), hydrogen atoms are excluded and the carbon atoms of the cycloheptyl ring are coloured red, both for clarity.

employed a cyclohexyl terminal group as this not only gave the highest clearing points (Table 1), simplifying study of smectic phases by SAXS, but also has zero ring strain.

Compounds **6** and **7** are non-mesogenic due to the short spacer between the end group and the core unit. Unlike **4**, which exhibits only a nematic phase, **8** and **9** both exhibit nematic and SmA phases. The enthalpy (and therefore entropy) associated with the N-SmA<sub>d</sub> transition is much larger for **9** than **8** and we will return to this point shortly. Compound **10** exhibits a direct Iso-SmA transition. All three phase transitions in Table 2 display a strong odd-even effect; transition temperatures are notably higher for odd parity materials. The smectic layer spacing of **9** was determined by SAXS, and presented as a

Table 2 Transition temperatures (*T*, °C) and associated enthalpies of transition ( $\Delta H$ , kJ mol<sup>-1</sup>) of cyclohexyl-terminated nOCB compounds

		MP	SmA <sub>d</sub> -N	N-Iso
<b>6</b>	<i>T</i>	120.8	—	—
( <i>n</i> = 1)	$\Delta H$	33.7	—	—
<b>7</b>	<i>T</i>	89.7	—	—
( <i>n</i> = 2)	$\Delta H$	27.4	—	—
<b>4</b>	<i>T</i>	94.8	—	84.0
( <i>n</i> = 3)	$\Delta H$	28.9	—	0.6
<b>8</b>	<i>T</i>	80.1	51.8	54.6
( <i>n</i> = 4)	$\Delta H$	34.6	0.4	0.4
<b>9</b>	<i>T</i>	97.8	82.7	85.3
( <i>n</i> = 5)	$\Delta H$	34.1	2.2	0.6
<b>10</b>	<i>T</i>	76.4	66.8	—
( <i>n</i> = 6)	$\Delta H$	25.0	2.2	—

*d/l* ratio using calculated molecular lengths (B3LYP/6-31G(d) level, 21.2 Å) as a function of reduced temperature in Fig. 3a. We also measured the layer spacings of two comparator materials, these were selected as they have approximately the same molecular length as compound **9** – 8OCB (*L* = 21.8 Å) and 2Si4OCB (*L* = 21.9 Å) – data are presented in Fig. 3a along with molecular structures (Fig. 3d, e).

Lastly, comparison of the diffuse wide-angle scattering peak of **9** and 8OCB reveals evidence for segregation into cycloalkyl rich sub-layers. Both **9** and 8OCB show a diffuse wide-angle peak at ~5 Å which results from the average lateral molecular separation. In the case of **9** an additional feature is present (Fig. 3f, *Q* ≈ 0.95 Å<sup>-1</sup>, *d* ≈ 6.6 Å); comparable features have been reported in siloxane liquid crystalline materials, and are interpreted as resulting from nanophase segregation.<sup>32</sup>

Typically the layer spacing of the SmA<sub>d</sub> phase is almost invariant with temperature,<sup>28</sup> however some materials with an acyclic 'bulky' group display temperature dependent layer spacing in the SmA<sub>d</sub> phase.<sup>5</sup> In the present study we observe the layer spacing of **9** to vary only slightly with temperature, however the *d/l* ratio is far larger than that of 8OCB (1.60 vs 1.43, respectively). The siloxane terminated material 2Si4OCB<sup>33</sup> exhibits a short range smectic A phase whose *d/l* ratio is intermediate between **9** and 8OCB. Study of compounds **8** and **10** by SAXS was complicated by crystallisation, however we were able to collect a single SAXS frame at temperatures of 44 °C and 65 °C, respectively. For **8** and **10** we measure layer spacings of 31.7 Å and 35.4 Å, respectively; this corresponds to *d/l* ratios of 1.61 for both materials. Of the materials studied by SAXS (**5**, **8**, **9**, **10**) we find the *d/l* ratios to be effectively identical.

It is known that cyanobiphenyl leads to antiparallel pairing through dipole-dipole interactions, increasing the effective length-to-breadth ratio (*i.e.* aspect ratio) and leading to interdigitated smectic phases.<sup>27,28</sup> To determine if this is a steric effect we devised compound **11**, a structural homologue of **9** however with an increased dipole moment (at the DFT(B3LYP/6-31G(d)) level: **9** = 7.2 Debye, **11** = 7.6 Debye) that might be





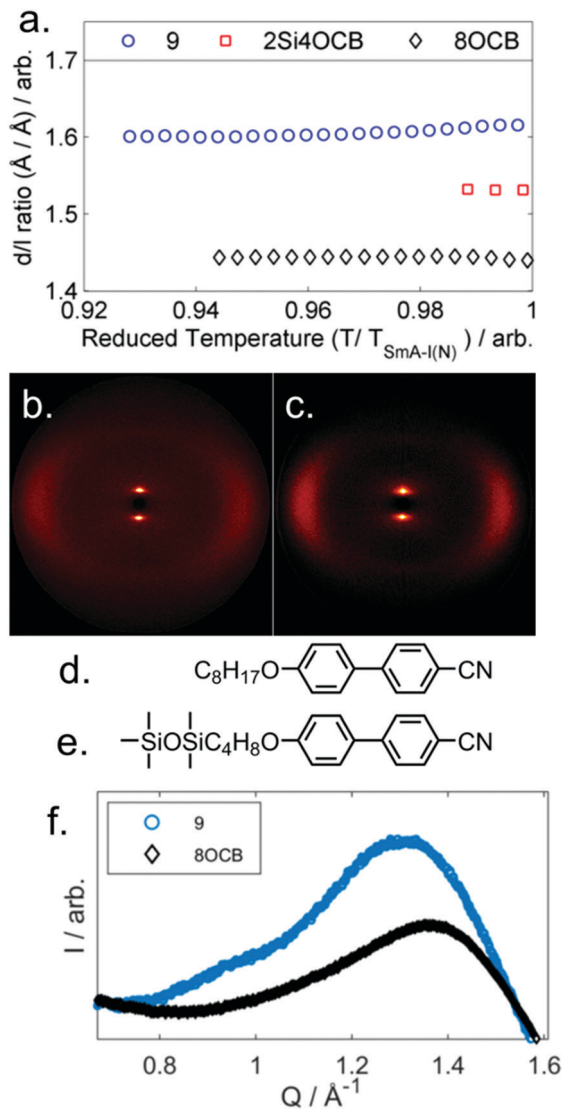


Fig. 3 (a) Plot of the  $d/l$  ratio of **9**, 2Si4OCB and 8OCB as a function of reduced temperature. Two-dimensional SAXS patterns for magnetically aligned samples of compounds **8** (b) and **9** (c) at a reduced temperature  $(T/T_{\text{SmA-N}})$  of 0.98. The molecular structures of 8OCB (Cr 54.5 SmA 67.2 N 80.0 Iso) and 2Si4OCB (Cr 39.7 (SmA 29.1) Iso) are given in (d) and (e), respectively. (f) Plot of scattered intensity ( $I$ ) as a function of the scattering vector ( $Q$ ,  $\text{\AA}^{-1}$ ) in the wide-angle region for **9** and 8OCB; note the additional feature present in **9** at  $Q \approx 0.95 \text{ \AA}^{-1}$ .

expected to alter the degree of antiparallel pairing and so lead to a change in layer spacing. If the effect is purely steric then the layer spacings should be unchanged. The transition temperatures and associated enthalpies of transition of **9** and **11** are given in Table 3.

The layer spacing of the SmA<sub>d</sub> phase of **11** was measured by SAXS (Fig. S1, ESI†) and was found to be temperature independent at 34.3  $\text{\AA}$ , corresponding to a  $d/l$  ratio of 1.60 using the molecular length of 21.4  $\text{\AA}$  (from geometry optimised at the B3LYP/6-31G(d) level). This result, which is the same as for compound **9**, supports the hypothesis that the enhancements to layer spacing and transition temperatures result from

Table 3 Comparison of Transition temperatures ( $T$ ,  $^{\circ}\text{C}$ ) and associated enthalpies ( $\Delta H$ ,  $\text{kJ mol}^{-1}$ ) of transition for cyclohexyl-terminated cyanobiphenyls with ether- (**9**) and ester- (**11**) linking groups

		MP	SmA <sub>d</sub> -N	N-Iso
<b>9</b>	$T$	97.8	82.7	85.3
	$\Delta H$	34.1	2.2	0.6
<b>11</b>	$T$	85.2	71.3	75.6
	$\Delta H$	34.1	0.1	0.9

segregation of the bulky end group *via* reducing the interpenetration of alkyl chains between adjacent smectic layers. In this scenario the antiparallel pairing of cyanobiphenyls is unperturbed by the cyclic end groups, with the increased layer spacing resulting from reduced layer interpenetration. Previously we have obtained values of the semi-empirical Kirkwood factor ( $g$ , effectively a measure of the degree of pairing in an anisotropic liquid) from measurement of the dielectric anisotropy coupled with calculated dipole moments and polarisabilities.<sup>27,34</sup> While this information would clearly be desirable for the present materials, the short nematic range of **9** and **11** leads to an unsaturated value of  $\Delta\epsilon$  and therefore of the Kirkwood factor.

We considered that the increase in smectic layer spacing when a bulky group is present could be caused by an increase in the orientational and/or translational order parameters. If we consider the change in layer spacing to be a consequence of size-exclusion effects similar to that observed in the solid state (Fig. 3), then we would expect no change in the orientational order parameters. We used the well-known method<sup>35–37</sup> to determine the orientational order parameters of **9** and 8OCB from the WAXS data, and they are presented in Fig. 4. The

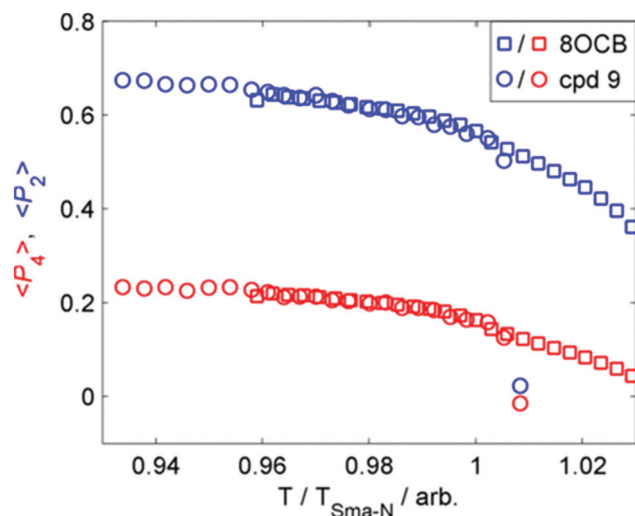


Fig. 4 Plot of the first two even  $\langle P_n \rangle$  order parameters as a function of reduced temperature  $(T/T_{\text{SmA-N}})$  for compound **9** (circles) and 8OCB (squares).



comparison of orientational order parameters in the nematic phase is complicated by the large difference in the temperature range of the nematic phase ( $\Delta T_{8OCB} \gg \Delta T_9$ ), however immediately prior to the SmA-N transition we find values of  $\langle P_2 \rangle$  and of  $\langle P_4 \rangle$  to be effectively the same for both materials. In the SmA phase we observe that at a given reduced temperature ( $T_{SmA-N}/T$ ) both materials have comparable values of  $\langle P_2 \rangle$  and  $\langle P_4 \rangle$ . The presence of a cyclic terminal group does not appear to affect the orientational order of the resulting mesophase, only the degree of positional order *via* segregation of the bulky cyclic terminal units. This effect can be considered as a steric pressure that results from the terminal group at the layer interface, reducing the interpenetration of aliphatic chains in adjacent layers and therefore giving increased layer spacing.

Fully atomistic molecular dynamics simulations were run on 8OCB and **9** to provide a comparison with the experimental data, and using a similar approach to that reported for 11OCB and *t*-Bu-11OCB (11OCB appended with a bulky tertiary butyl end-group).<sup>38</sup> The simulations were run from isotropic liquid-phase starting geometries of 1440 molecules and at a reduced temperature of  $T/T_c = 0.934$  for both systems, where  $T_c$  is the estimated clearing point of the respective simulated system; the corresponding experimental temperatures are 56.7 and 61.6 °C ( $T/T_{SmA-N} = 0.970$  and 0.941) for 8OCB and **9**, respectively. Details of the methods are given in the ESI.†

Both simulated systems evolved to form a smectic A phase. The evolution of the orientational order parameters  $P_2$  and  $P_4$ , obtained using the N–O vector as the principal axis, are shown in Fig. 5. The evolution of the translational order parameter  $\tau$  and associated layer spacing  $d$ , obtained using the  $C_4'$  biphenyl carbon atom to define the molecular position, are shown in Fig. 6. An analysis of the angle between the director and the layer normal, presented in the ESI,† confirmed that both simulated systems formed a smectic A phase. The simulated smectic A phase of 8OCB formed relatively quickly (*ca.* 60 ns) but was typically not stable (beyond *ca.* 200 ns), whereas that of **9** formed more slowly (*ca.* 200 ns) and was more stable (to at least 1000 ns). We attribute the behaviour of 8OCB to the ready formation of diffuse layers in a simulation that lacks long-term stability due to the use of anisotropic pressure coupling, which allows the simulation box aspect ratios to vary and avoids bias from a constrained box shape but which results in an unstable simulation box and phase for this system. By contrast, we attribute the behaviour of **9** to the bulky end-group leading to the slower formation of more ordered layers that give a more stable simulation once formed.

In comparison with the respective experimental data at the relevant temperature, these simulated phases give average  $P_2$  values that are closely similar, average  $P_4$  values that are slightly higher, and average  $d$  values that are closely similar. We do not have experimental data for a comparison with the average  $\tau$  values, but together the available comparisons suggest that the simulations may reasonably be used as an aid to interpret the experimental data.

Fig. 7 shows snapshots from the simulations of 8OCB and **9** at times when the layers are relatively well-defined, with each

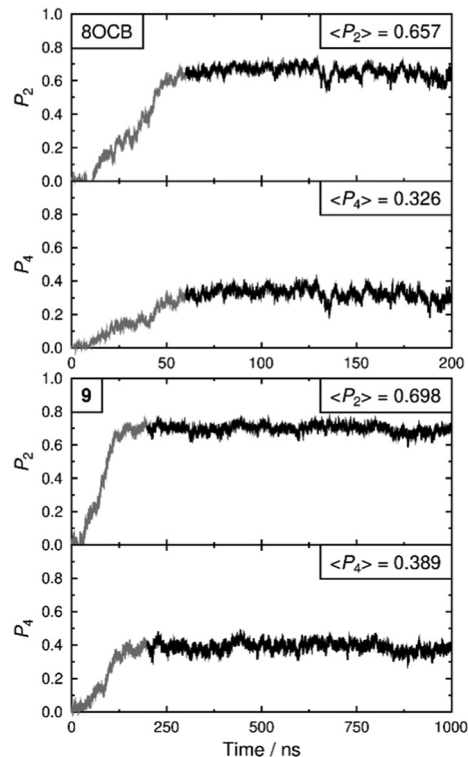


Fig. 5 Orientational order parameters,  $P_2$  and  $P_4$ , from the MD simulations of 8OCB (top) and **9** (bottom) vs. time. The average values given in the insets were determined over the region of each simulation represented by the heavier lines (60–200 ns and 200–1000 ns, respectively).

molecule represented by a cylinder that corresponds to the N–O molecular vector, *i.e.* the relatively rigid aromatic moiety, used to determine the orientational order parameters. For 8OCB, the layers are not very well defined, as indicated also by the relatively low value of  $\tau$ , and some of the layers show large ripples. By contrast, the layers of **9** are more clearly defined and flatter, with the empty regions between the layers of cylinders in this snapshot containing the cyclohexyl- $C_5$  chains (not shown in this snapshot for clarity). Moreover, an examination of the density of layered atoms along the layer normal vector (comparable to the director) over time showed that the layers of 8OCB often formed for short periods of *ca.* 10–20 ns before breaking up and then reforming at other locations along the layer normal vector at later times, whereas the layers of **9** remained comparatively stable in location once formed.

The structures of the phases were also assessed using pairwise correlation functions<sup>39</sup> of vectors between the  $C_4$  and  $C_4'$  biphenyl atoms on all of the molecules, as shown in Fig. 8. The radial distribution function  $g(r)$  used the centres of the biphenyl vectors, and shows liquid-like distributions with peaks at *ca.* 5.1 and 9.9 Å for both 8OCB and **9**, corresponding to “shells” of surrounding molecules, and tending towards 1 at longer distances indicating long-range disorder; the slightly higher  $g(r)$  values for **9** than 8OCB are consistent with a slightly more ordered phase. The first-order orientational correlation functions  $G_1(r)$  of the biphenyl vectors in 8OCB and **9** both show a



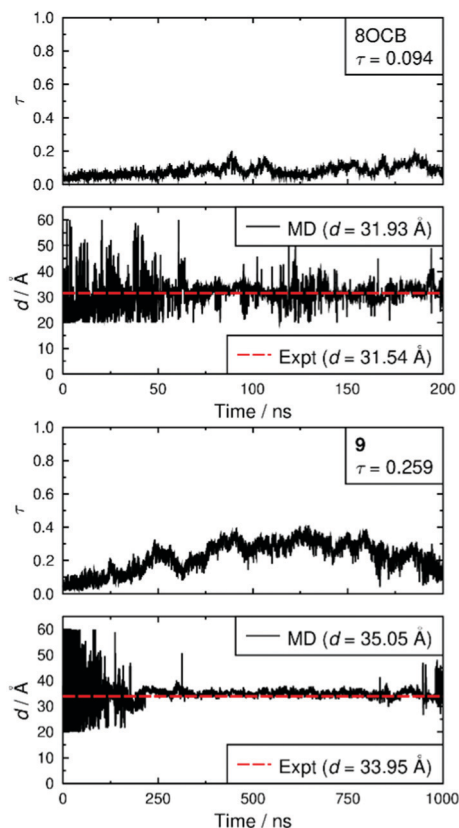


Fig. 6 Translational order parameters,  $\tau$ , and layer spacings,  $d$ , from the MD simulations of 8OCB (top) and **9** (bottom). The average MD values given in the insets were determined over times 60–200 ns and 200–1000 ns for 8OCB and **9**, respectively, once the phase had formed and was relatively stable. The experimental values of  $d$  are given for the closest temperatures at which SAXS data were recorded (56.74 and 61.69 °C, respectively).

negative peak at *ca.* 3–4 Å corresponding to antiparallel molecular orientations of the biphenyl units being favoured in the

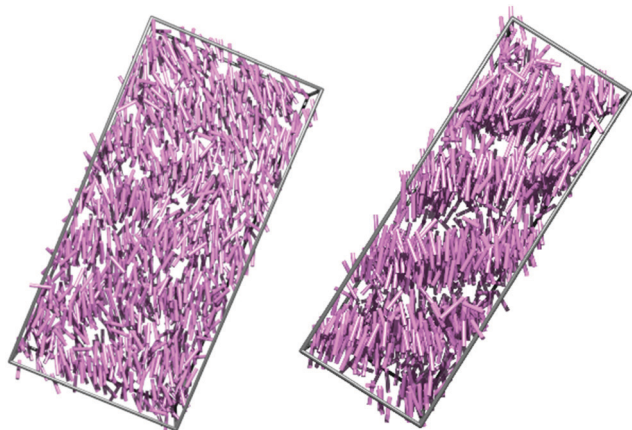


Fig. 7 Snapshots of the simulations of 8OCB at 75 ns (left) and **9** at 646 ns (right), each shown at a time after layer formation has occurred and oriented with the layer normal vector vertical. The purple cylinders representing the molecules are drawn between the nitrogen and oxygen atoms, and the boundaries of the simulation boxes are shown in grey.

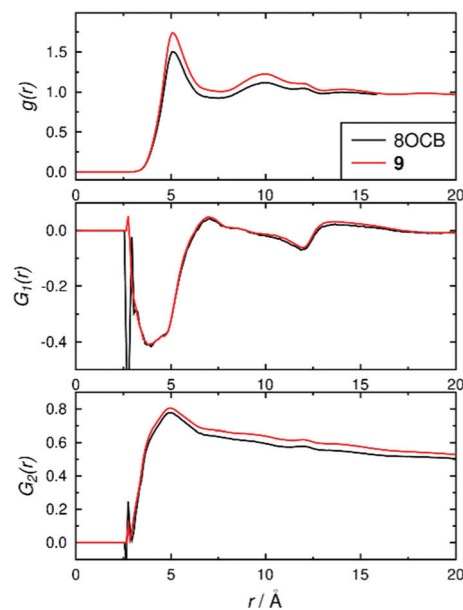


Fig. 8 Pair-wise correlation functions determined over the time ranges 60–200 ns for 8OCB and 200–1000 ns for **9**.

first shell, and a weaker positive peak at *ca.* 7 Å corresponding to parallel molecular orientations being favoured more weakly in the next shell (as illustrated schematically in Fig. 2 c and d); this observation is consistent with those reported from simulations of other related *n*CB and *n*OCB systems.<sup>39,40</sup> The second-order orientational correlation function  $G_2(r)$  used the same biphenyl reference vector, and shows a peak at *ca.* 5 Å indicating a very high  $P_2$  orientational order in the first shell that decreases towards values of  $\langle P_2 \rangle^2$  at longer distances, as expected.<sup>39</sup> Taken together, the distribution functions in Fig. 8 show that the ordering behaviour of the biphenyl groups of 8OCB and **9** are similar, which suggests that the differences in smectic layer formation and stability are strongly influenced by the nature of the alkyl chains at the other ends of these molecules.

The extent of layering and interdigitation of the molecules was assessed using a similar approach to that reported for 11OCB and *t*-Bu-11OCB.<sup>38</sup> Fig. 9 shows the relative populations along the layer normal vector,  $z$ , of a selected head-group atom ( $C_4'$  biphenyl for both 8OCB and **9**, as used to determine  $\tau$  values) and a selected tail-group atom (the terminal carbon atom;  $C_8$  alkyl for 8OCB, and  $C_4$  cyclohexyl for **9**) during a 50 ns window when the layer positions were relatively stable in each simulation box. All of the relative populations have an approximately sinusoidal form, as shown by the black lines in Fig. 9, with the populations of the head-group and tail-group atoms being out of phase, which indicates the presence of distinct aromatic and aliphatic regions along the layer normal. The amplitude of the oscillations is low for 8OCB, illustrating the diffuse nature of the layers, and much higher for **9**, showing the greater degree of nanosegregation between its aromatic and aliphatic moieties.





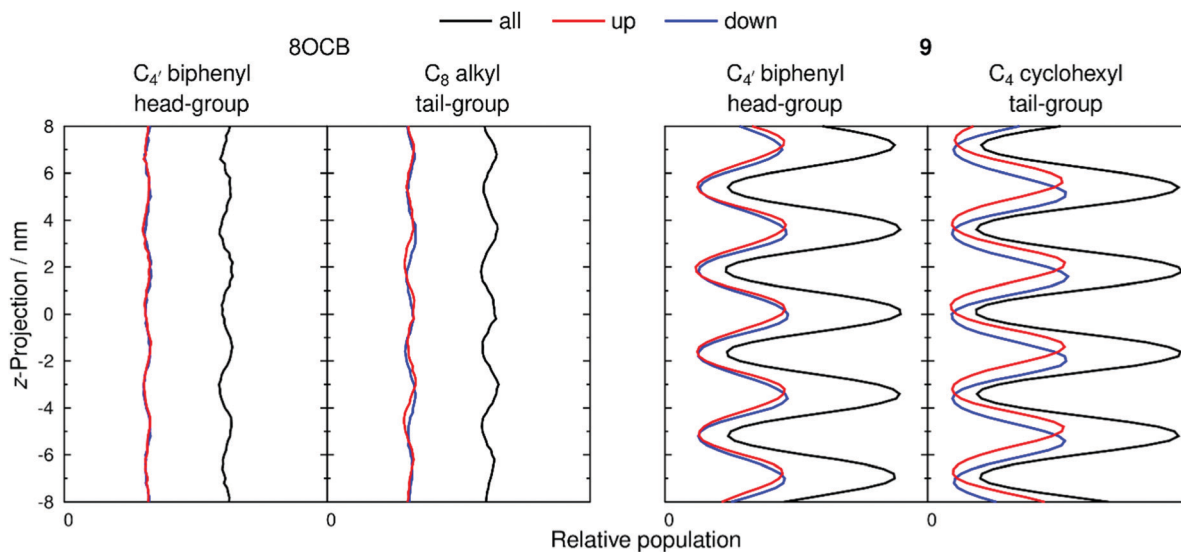


Fig. 9 Relative populations along the layer normal,  $z$ , of head-group and tail-group atoms of 8OCB (left) and **9** (right), calculated over a 50 ns period of each simulation (100–150 ns and 600–650 ns, respectively) and generated with 0.2 nm bin-widths. Black lines show the positions for all molecules, whereas red and blue lines represent molecules pointing up and down, respectively. The  $z$ -projection was defined as zero at the centre of the simulation box and population scales are consistent between plots.

Fig. 9 also shows the relative populations for molecules with the C–N vector pointing “up” (red) or “down” (blue) along the  $z$ -axis, which corresponds to molecules having their alkyl chains below or above the aromatic moiety, respectively, along this axis (as illustrated schematically in Fig. 2 c and d). In Fig. 9, the head-group atoms of 8OCB and **9**, and the tail-group atoms of 8OCB, show only a small difference in the relative populations of the “up” and “down” molecules along the  $z$ -axis, which indicates a significant degree of interdigitation of the aromatic head-groups of 8OCB and **9**, and of the linear alkyl tail groups of 8OCB. By contrast, the cyclic tail-group atoms of **9** show relative populations of “up” and “down” molecules that are distinctly offset along the  $z$ -axis, with the “up” molecules (cyclohexyl group at the bottom) being higher on the  $z$ -axis than that of the “down” molecules (cyclohexyl group at the top), which indicates a relatively low degree of interdigitation for the cyclic tail groups of **9**.

The distributions shown in Fig. 9 were used to quantify the extent of interdigitation.<sup>38</sup> The C<sub>4</sub>' biphenyl head group atoms of 8OCB and **9** showed 50% and 53% interdigitation, respectively, corresponding to approximately half of these head-group atoms being located in the adjacent layer. The C<sub>8</sub> alkyl tail group atoms of 8OCB showed 50% interdigitation, similar to the head groups, whereas the C<sub>4</sub> cyclohexyl tail group atoms of **9** showed a much lower interdigitation of 39%. Hence, 8OCB shows a similar extent of interdigitation at both ends of the molecule, whereas **9** shows much less interdigitation of the bulky cyclohexyl tail group than the biphenyl head group. This behaviour is similar to that reported previously for 11OCB and *t*-Bu-11OCB,<sup>38</sup> where the bulky *t*-Bu tail group displayed less interdigitation than the other terminal groups in either system.

The difference in the extent of interdigitation between 8OCB and **9** suggests that the inter-layer boundary at the tail end of

these molecules is more clearly defined for **9** than 8OCB. This effect is shown clearly by the snapshots in Fig. 10, which show the positions and orientations of the five terminal carbon atoms of the alkyl chain of 8OCB and the equivalent carbon atoms of **9**. For 8OCB, there is clear interdigitation between the alkyl chains of the molecules pointing up and down, and the associated alkyl layers are diffuse. For **9**, not only are the alkyl layers more defined, but the inter-layer boundary shows two almost distinct sub-layers arising from the separation of cyclohexyl groups in molecules pointing up and down.

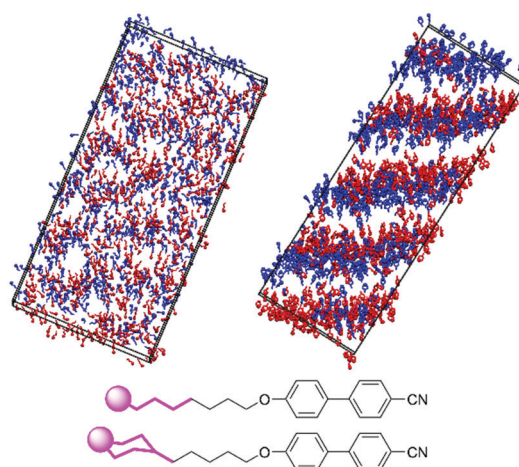


Fig. 10 Snapshots of the simulations of 8OCB at 75 ns (left) and **9** at 646 ns (right) showing the terminal alkyl carbon atoms from C<sub>4</sub> onwards, as shown in bold on the structures (bottom); the terminal carbon atoms are represented by spheres to assist orientation. Up and down molecules are coloured red and blue, respectively, and the simulation boxes are oriented with the layer normal vector vertical.





## Conclusions

We have expanded on our previous work using bulky terminal groups to promote the SmA phase in cyanobiphenyl mesogens by using terminal cyclic groups separated from the core using relatively short aliphatic chains. The enhancement to smectic layer spacing observed in cyanobiphenyl materials with bulky terminal groups is a steric effect, and occurs without change in orientational order parameter. Provided a bulky group is present, the layer spacing is  $\sim 1.6$  times the molecular length regardless of terminal ring size (5), alkyl chain length (8, 9 and 10) and linking group (9 and 11). This effect can be exploited to give significant increases to the onset transition temperature of both nematic and smectic mesophases, as demonstrated by comparing compound 9 to its linear analogue. Results from fully atomistic MD simulations support the overall interpretation from experiment that a cyclic end-group on the alkyl chain reduces the interpenetration of molecules between smectic layers in these systems. This phenomenon points to a potentially new method for stabilising both nematic and smectic liquid-crystalline states should the accompanying increase in melting points be countered.

## Data availability

Raw data pertinent to this work is available on request from the University of York data catalogue. Crystal structure data for compounds 1–5 is deposited with the CCDC (deposition numbers 2128187, 2128188, 2128189, 2128190 and 2128191, respectively).

## Conflicts of interest

There are no conflicts to declare.

## Acknowledgements

The authors wish to thank the EPSRC for funding through grants EP/M020584/1 and EP/K039660/1. LF acknowledges funding by the Coordenação de Aperfeiçoamento de Pessoal de Nível Superior, Brazil (CAPES), finance code 001. We thank Dr Chris Rhodes of the University of York for designing and constructing the LED photoreactor used in the synthesis of compound 2. We thank the referees for suggestions regarding the detection of segregation effects in X-ray scattering data.

## References

- 1 T. V. Clapp, W. A. Crossland, A. B. Davey, M. Grasmann, J. P. Hannington, R. K. King, M. Pivnenko, S. Robson and H. Xu, *US Pat*, 8956548, 2015.
- 2 D. J. Gardiner and H. J. Coles, *J. Phys. D: Appl. Phys.*, 2006, **39**, 4948–4955.
- 3 J. P. Hannington, T. V. Clapp, F. Nishida, R. K. King, O. Farooq, M. Grasmann, W. A. Crossland, H. J. Coles, A. B. Davey, H. Xu, O. Haderler and M. Pivnenko, *United States Patent No. 8821992*, 2014.
- 4 R. J. Mandle, E. J. Davis, J. P. Sarju, N. Stock, M. S. Cooke, S. A. Lobato, S. J. Cowling and J. W. Goodby, *J. Mater. Chem. C*, 2015, **3**, 4333–4344.
- 5 R. J. Mandle, E. J. Davis, C. C. A. Voll, D. J. Lewis, S. J. Cowling and J. W. Goodby, *J. Mater. Chem. C*, 2015, **3**, 2380–2388.
- 6 K. M. Mulligan, A. Bogner, Q. X. Song, C. P. J. Schubert, F. Giesselmann and R. P. Lemieux, *J. Mater. Chem. C*, 2014, **2**, 8270–8276.
- 7 C. P. J. Schubert, A. Bogner, J. H. Porada, K. Ayub, T. Andrea, F. Giesselmann and R. P. Lemieux, *J. Mater. Chem. C*, 2014, **2**, 4581–4589.
- 8 E. J. Davis, R. J. Mandle, B. K. Russell, P. Y. Foeller, M. S. Cook, S. J. Cowling and J. W. Goodby, *Liq. Cryst.*, 2014, **41**, 1635–1646.
- 9 I. Rupar, K. M. Mulligan, J. C. Roberts, D. Nonnenmacher, F. Giesselmann and R. P. Lemieux, *J. Mater. Chem. C*, 2013, **1**, 3729–3735.
- 10 D. L. Valentine, *Nat. Rev. Microbiol.*, 2007, **5**, 316–323.
- 11 K. O. Stetter, *Philos. Trans. R. Soc., B*, 2006, **361**, 1837–1842.
- 12 A. Gliozzi, G. Paoli, M. Derosa and A. Gambacorta, *Biochim. Biophys. Acta, Biomembr.*, 1983, **735**, 234–242.
- 13 Y. Koga, *Archaea*, 2012, 789652, DOI: 10.1155/2012/789652.
- 14 J. S. S. Damste, S. Schouten, E. C. Hopmans, A. C. T. van Duin and J. A. J. Geenevasen, *J. Lipid Res.*, 2002, **43**, 1641–1651.
- 15 G. Lecollinet, A. Gulik, G. Mackenzie, J. W. Goodby, T. Benvegnu and D. Plusquellec, *Chem. – Eur. J.*, 2002, **8**, 585–593.
- 16 S. J. Cowling, A. W. Hall and J. W. Goodby, *Liq. Cryst.*, 2005, **32**, 1483–1498.
- 17 S. J. Cowling and J. W. Goodby, *Chem. Commun.*, 2006, 4107–4109, DOI: 10.1039/b610154b.
- 18 J. Furukawa, N. Kawabata and J. Nishimura, *Tetrahedron*, 1968, **24**, 53–58.
- 19 C. P. Johnston, R. T. Smith, S. Allmendinger and D. W. C. MacMillan, *Nature*, 2016, **536**, 322–325.
- 20 O. Mitsunobu and M. Yamada, *Bull. Chem. Soc. Jpn.*, 1967, **40**, 2380–2382.
- 21 T. Qin, J. Cornella, C. Li, L. R. Malins, J. T. Edwards, S. Kawamura, B. D. Maxwell, M. D. Eastgate and P. S. Baran, *Science*, 2016, **352**, 801–805.
- 22 L. J. Perez, W. L. Ng, P. Marano, K. Brook, B. L. Bassler and M. F. Semmelhack, *J. Med. Chem.*, 2012, **55**, 9669–9681.
- 23 Y. F. Tian, A. B. Ling, R. Fang, R. X. Tan and Z. Q. Liu, *Green Chem.*, 2018, **20**, 3432–3435.
- 24 M. J. Frisch, G. W. Trucks, H. B. Schlegel, G. E. Scuseria, M. A. Robb, J. R. Cheeseman, G. Scalmani, V. Barone, B. Mennucci, G. A. Petersson, H. Nakatsuji, M. Caricato, X. Li, H. P. Hratchian, A. F. Izmaylov, J. Bloino, G. Zheng, J. L. Sonnenberg, M. Hada, M. Ehara, K. Toyota, R. Fukuda, J. Hasegawa, M. Ishida, T. Nakajima, Y. Honda, O. Kitao, H. Nakai, T. Vreven, J. A. Montgomery Jr., J. E. Peralta, F. Ogliaro, M. J. Bearpark, J. Heyd, E. N. Brothers, K. N. Kudin, V. N. Staroverov, R. Kobayashi, J. Normand, K. Raghavachari, A. P. Rendell, J. C. Burant, S. S. Iyengar,



- J. Tomasi, M. Cossi, N. Rega, N. J. Millam, M. Klene, J. E. Knox, J. B. Cross, V. Bakken, C. Adamo, J. Jaramillo, R. Gomperts, R. E. Stratmann, O. Yazyev, A. J. Austin, R. Cammi, C. Pomelli, J. W. Ochterski, R. L. Martin, K. Morokuma, V. G. Zakrzewski, G. A. Voth, P. Salvador, J. J. Dannenberg, S. Dapprich, A. D. Daniels, Ö. Farkas, J. B. Foresman, J. V. Ortiz, J. Cioslowski and D. J. Fox, *Gaussian 09 rev E.01*, 2009.
- 25 W. Humphrey, A. Dalke and K. Schulten, *J. Mol. Graphics Modell.*, 1996, **14**, 33–38.
- 26 M. Tarini, P. Cignoni and C. Montani, *IEEE Trans. Vis. Comput. Graph.*, 2006, **12**, 1237–1244.
- 27 R. J. Mandle, S. J. Cowling, I. Sage, M. E. Colclough and J. W. Goodby, *J. Phys. Chem. B*, 2015, **119**, 3273–3280.
- 28 A. J. Leadbetter, J. C. Frost, J. P. Gaughan, G. W. Gray and A. Mosley, *J. Phys.*, 1979, **40**, 375–380.
- 29 A. LeCalvez, S. Montant, E. Freysz, A. Ducasse, X. W. Zhuang and Y. R. Shen, *Chem. Phys. Lett.*, 1996, **258**, 620–625.
- 30 S. Maisch, A.-M. Krause, D. Schmidt and M. Lehmann, *Liq. Cryst.*, 2017, 1–16, DOI: 10.1080/02678292.2017.1369595.
- 31 J. W. Goodby, R. J. Mandle, E. J. Davis, T. Zhong and S. J. Cowling, *Liq. Cryst.*, 2015, **42**, 593–622.
- 32 D. M. Agra-Kooijman, H. Yoon, S. Dey and S. Kumar, *Phys. Rev. E: Stat., Nonlinear, Soft Matter Phys.*, 2014, **89**, 032506.
- 33 R. J. Mandle and J. W. Goodby, *React. Chem. Eng.*, 2018, **3**, 515–519.
- 34 R. J. Mandle and J. W. Goodby, *Liq. Cryst.*, 2017, **44**, 656–665.
- 35 P. Davidson, D. Petermann and A. M. Levelut, *J. Phys. II*, 1995, **5**, 113–131.
- 36 M. T. Sims, L. C. Abbott, R. M. Richardson, J. W. Goodby and J. N. Moore, *Liq. Cryst.*, 2018, **46**, 11–24.
- 37 D. M. Agra-Kooijman, M. R. Fisch and S. Kumar, *Liq. Cryst.*, 2018, **45**, 680–686.
- 38 M. T. Sims, L. C. Abbott, J. W. Goodby and J. N. Moore, *Soft Matter*, 2019, **15**, 7722–7732.
- 39 M. F. Palermo, A. Pizzirusso, L. Muccioli and C. Zannoni, *J. Chem. Phys.*, 2013, **138**, 204901.
- 40 R. Pecheanu and N. M. Cann, *Phys. Rev. E: Stat., Nonlinear, Soft Matter Phys.*, 2010, **81**, 041704.

